Chapter 4

Microstructure of bulk nanostructured steel

4.1 Introduction

Nanostructured bainite is generally produced in high carbon low alloy steels by isothermally transforming at the lowest possible temperatures [120]. This particular steel has garnered much attention due to its high strength and toughness [71,183]. The high strength level of bainite generally comes from its fine plates [75,76]. The thickness of bainite plates increases with driving force ($\Delta G^{\gamma\rightarrow\alpha}$) and temperature of transformation, but it decreases with an enhanced yield strength of austenite (σ^{γ}) [77,78]. There is sufficient evidence that bainite is plastically accommodated in the austenite phase due to transformation at higher temperatures [77,81]. Dislocations generated in austenite through plastic accommodation during transformation can contribute to the refinement of bainite plates by increasing the yield strength of austenite. However, empirical equations developed to predict the plate thickness do not take into account the effect of dislocation density. This chapter focuses on effect of dislocation density on bainite plate thickness with varying austempering time.

Diffusionless transformation products like bainite exhibit a specific orientation relationship with the parent phase [75]. The OR can approximately be either Kurdjumov–Sachs (K-S) [47] or Nishiyama–Wasserman (N-W) [87] type, depending on the processing conditions [88]. There are 24 K-S variants possible for a single austenite grain (V1-V24) [90]. This chapter also shows dominant variant pairing with the austempering time.

4.2 Results

Fig. 3 displays optical micrographs of the austempered samples. The black and white regions represent bainite sheaves (α_b), and retained austenite (RA) as shown in the optical micrograph of D2-25h in Fig. 4.1a. As the holding time increases from 25 hours to 33 hours and 48 hours, the amount of bainite in the D2-33h (Fig. 4.1b) and D2-48h (Fig. 4.1c) samples increases, but the difference is not significant. The volume fraction of bainite and austenite

phases is determined using an EBSD phase map. The D2-25h sample shows 35.5% bainite (Fig.4.1d), which increases to 53% in the D2-33h (Fig.4.1e). Interestingly, the D2-48h sample (Fig.4.1f) only contains 59% bainite phase, despite the longer austempering time.

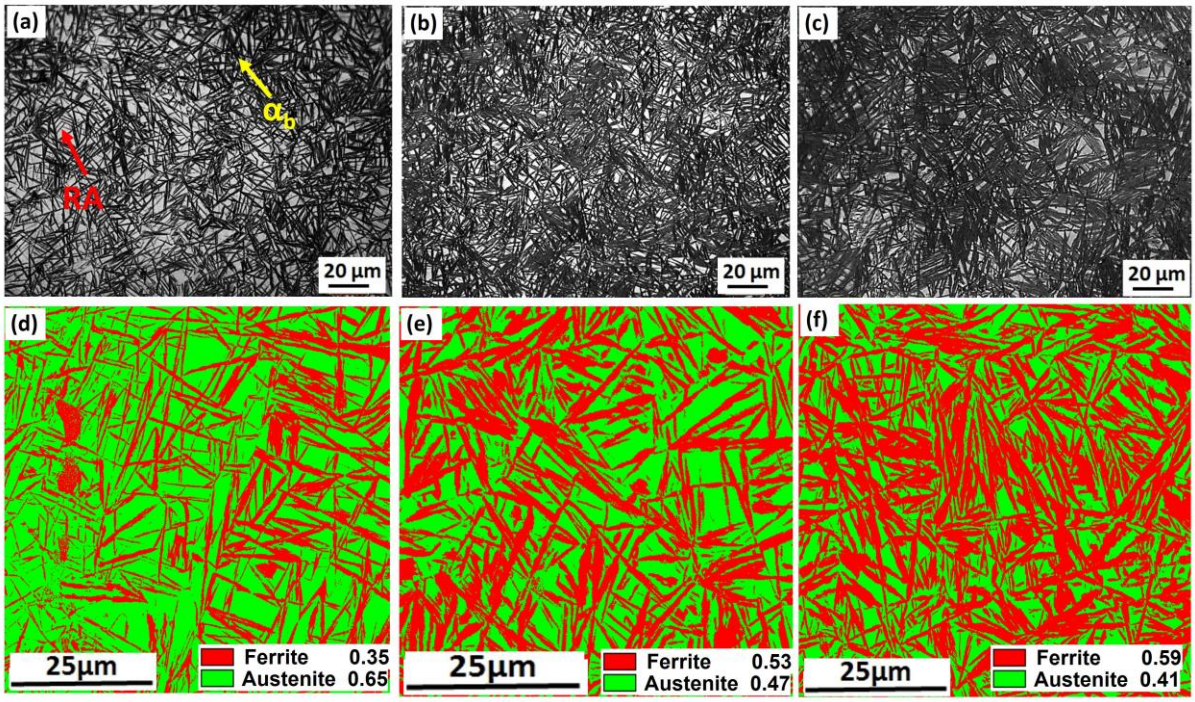

Figure 4.1. *Optical micrographs of (a) D2-25h, (b) D2-33h and (c) D2-48h and EBSD phase maps of (d) D2-25h, (e) D2-33h and (f) D2-48h. (α_b and RA stand for bainite, retained austenite respectively).*

Higher magnification SEM images of the D2-25h, D2-33h, and D2-48h samples are presented in Figures 4.2a, b, and c, respectively. The apparent thickness of bainite plates is measured, and the corresponding histogram is shown in Figures 4.2d, e, and f for D2-25h, D2-33h, and D2-48h samples, respectively. The average thickness of bainite plates is determined to be 51±18 nm, 53±20 nm, and 65±34 nm for D2-25h, D2-33h, and D2-48h samples.

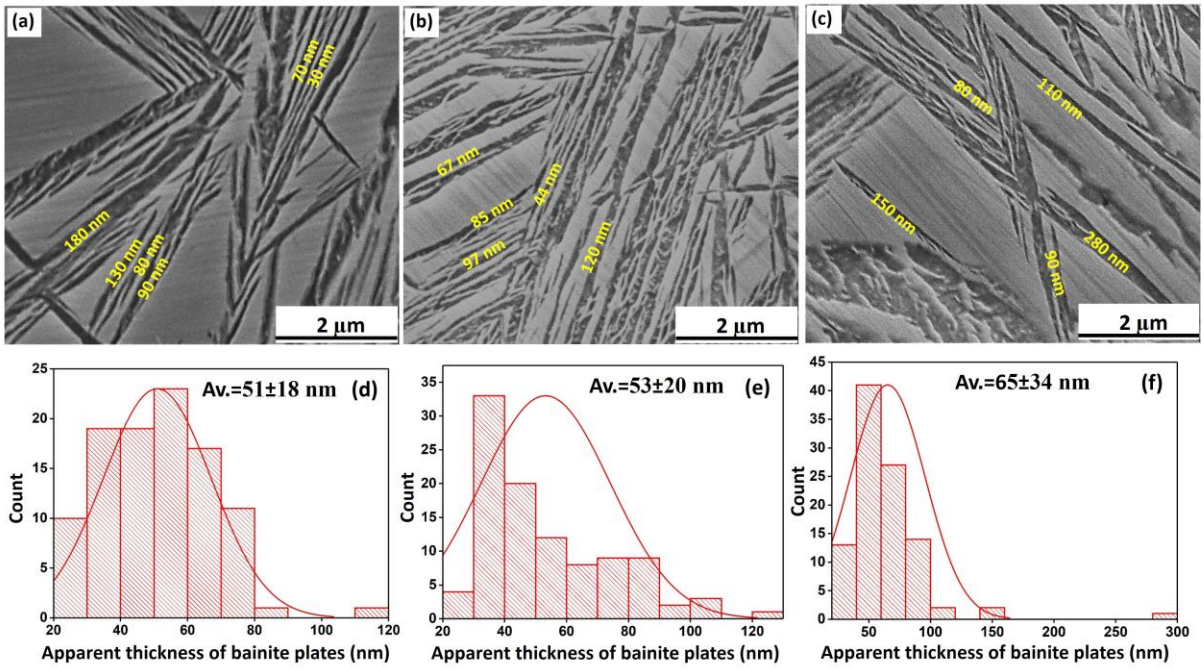

Figure 4.2. *SEM secondary electron micrographs at higher magnifications of (a) D2-25h, (b) D2-33h, and (c) D2-48h, the corresponding histogram for apparent plate thickness of (d) D2-25h, (e) D2-33h and (f) D2-48h.*

The phases in the XRD peaks are identified based on the ICDD, PDF2 database and are marked on the peaks with their corresponding diffracting planes (Fig. 4.3a, b and c). Rietveld refinement of XRD patterns is carried out, considering bainite and austenite as a BCC (Im-3m) and FCC (Fm-3m) structures, respectively. The lattice parameters of bainite and retained austenite in D2-25h are estimated using the Rietveld refinement technique to be 2.876±0.002 Å and 3.619±0.002 Å, respectively (Table 4.1). On increasing the austempering time to 33 hours, the lattice parameter of bainite remains the same 2.876±0.002 Å, but further austempering for 48 hours leads to a minor decrease in bainite lattice parameter to 2.873±0.0012 Å. The lattice parameter of austenite in the D2-33h and d2-48h samples increases to 3.622±0.001 Å and 3.623±0.001 Å, respectively (Table 4.1). Carbon content in retained austenite and bainite are calculated from equations given in experimental section. Carbon enrichment in the austenite phase of D2-25h is calculated to be 1.07±0.03 mass %, which increases to 1.13±0.02 mass % and 1.15±0.015 mass % in D2-33h and D2-48h, respectively.

The carbon content of bainite phase of D2-25h and D2-33h is same value of 0.21±0.03 mass % in the sample. However, after a longer isothermal holding (D2-48h), the carbon content decreases to 0.12±0.02 mass %.

The volume percent of bainite and retained austenite are estimated from the fitted intensity plots using the Rietveld refinement technique. The volume percent of bainite in D2-25h is 35±2%, which increases to 50±2% after 33 hours of austempering. However, surprisingly, when increasing the austempering time to 48 hours (D2-48h), the amount of bainite only increases to 54±1% (Table 4.1). Even after an additional 15 hours of austempering, only 6±2% extra volume percent of bainite is formed. This suggests that the transformation has nearly reached its saturation limit.

The intensity distribution of the (111) peak of retained austenite in D2-25h is asymmetric, whereas it is more symmetric in D2-48h, and the said peak is shifted towards lower Bragg angles (Fig. 4.3d). The asymmetric peak of the D2-25h sample is mainly due to the inhomogeneous carbon distribution in filmy and blocky retained austenite, which progressively decreases as the transformation time increases to 33 hours and 48 hours as shown in Fig.4.3d.

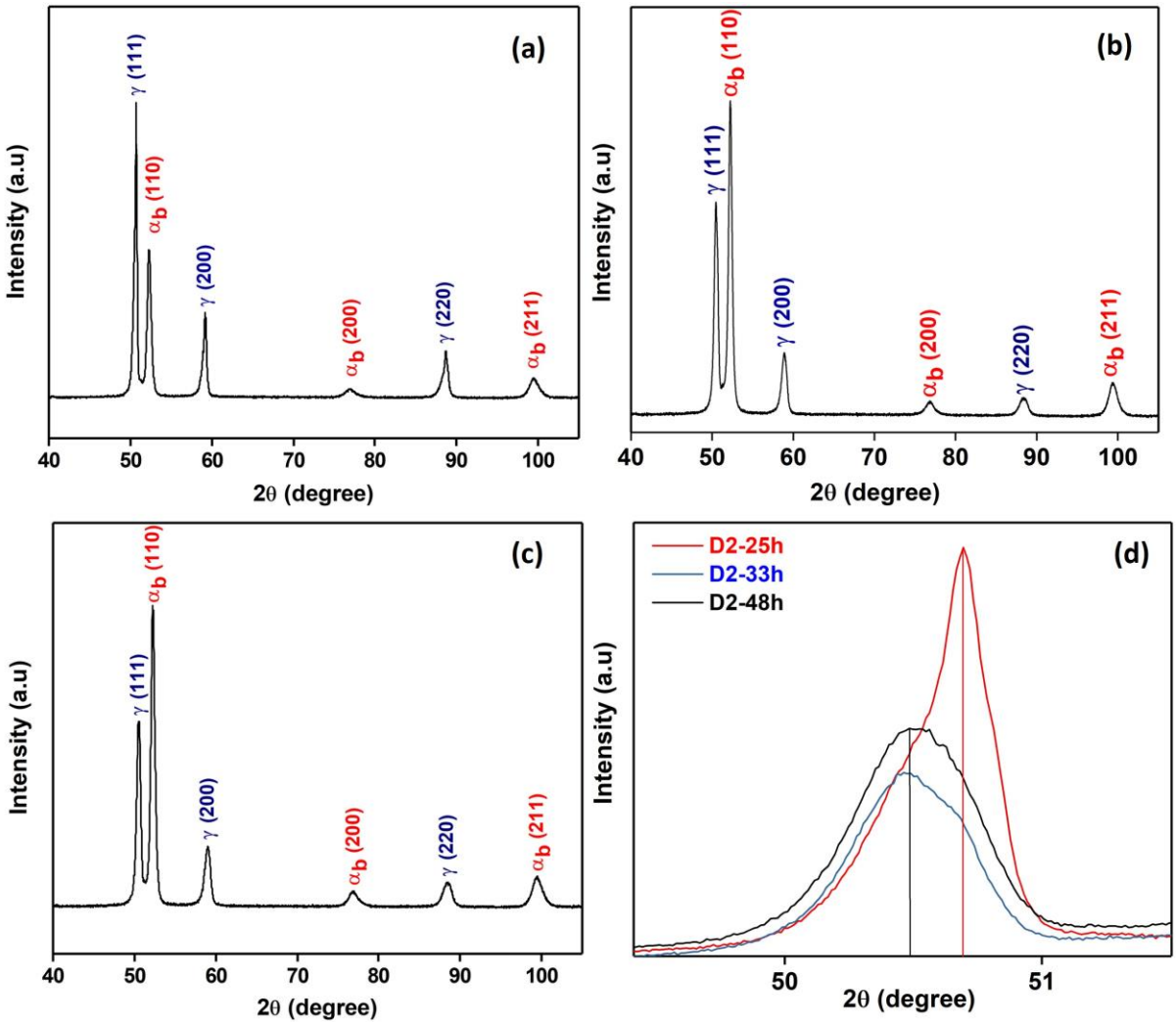

Figure 4.3. *XRD patterns of (a) D2-25h, (b) D2-33h, (c) D2-48h, (d) (111) austenite peaks and (γ and α_b denotes austenite and bainite phases respectively)*

Table 4.1. Estimated lattice parameter, carbon content, volume fraction obtained by Rietveld refinement.

Sample	a_γ (Å)	Carbon content in Austenite (mass %)	a_α (Å)	Carbon content in Bainite (mass %)	V_α (%)
D2-25h	3.619±0.002	1.07±0.03	2.876±0.002	0.21±0.03	35±2
D2-33h	3.622±0.001	1.13±0.02	2.876±0.0015	0.21±0.03	50±2
D2-48h	3.623±0.001	1.15±0.015	2.873±0.0012	0.12±0.02	54±1

The crystallite size of bainite in D2-25h is 137±31 Å. On increasing the austempering time to 33 hours, the crystallite size marginally increases to 141±33 Å (Table 4.2), and after 48 h of

austempering it further increases to 152±41 Å. The crystallite size of the retained austenite decreases with the decrease in its volume fraction and due to shape deformation caused by bainite transformation (Table 4.2). The initial micro-strain in the retained austenite phase of the transformed sample (D2-25h) is 0.5±0.09%. After further austempering to 33 hours and 48 hours, the micro-strain slightly increases to 0.55±0.09% (Table 4.2) due to formation of more amount of bainite and filmy austenite. Strain due to bainite is higher in the filmy retained austenite compared to blocky retained austenite as the central portion in the latter case experiences minimum transformation related effects [96,184]. In the case of the bainite phase, the micro-strain in D2-25h sample decreases slightly from 0.518±0.08% to 0.5±0.08% and 0.48±0.07% after 33 hours and 48 hours of austempering respectively. The dislocation density in the bainite phase of the D2-25h sample is estimated to be 28±4 x $10^{15}/m^2$ using the modified Williamson-Hall method, which slightly decreases as austempering time increases to 33 hours and 48 hours. The dislocation density in the retained austenite of D2-25h is 4.1±0.8 x $10^{15}/m^2$, which remains in the same level after 33 hours of transformation, but decreases significantly to 2.2±0.6 x $10^{15}/m^2$ (Table 4.2) after 48 hours of austempering.

Table 4.2. XRD line profile analysis results for crystallite size, micro-strain, and dislocation density.

Sample		Crystallite Size (Å)	Micro-Strain (%)	Dislocation density (x $10^{15}/m^2$)
D2-25h	Bainite	137±31	0.52±0.08	28±4
	Austenite	153±42	0.50±0.09	4.1±0.8
D2-33h	Bainite	141±33	0.5±0.08	26.5±3
	Austenite	148±45	0.56±0.09	4.4±0.6
D2-48h	Bainite	152±41	0.48±0.07	26±3
	Austenite	137±39	0.55±0.09	2.2±0.6

The KAM map, depicted in Figure 4.4, provides qualitative information regarding strain and dislocation density. A single austenite grain is selected from the original scan data, and the strain is shown using the 3rd nearest neighbor at the perimeter with a maximum misorientation angle of 5°. The legend at the bottom of the figure illustrates the variation of strain at different locations. The KAM map of the RA phase shows that the strain in the initial sample (D2-25h) (Figure 4.4a) of 0.85° decreases to 0.8° and 0.56°, respectively as the austempering time increases from 25 hours to 33 hours (Figure 4.4b) and then to 48 hours (Figure 4.4c). The strain in the bainite phase remains constant for the D2-25h (Figure 4.4d) and D2-33h samples (Figure 4.4e), but it decreases significantly to 0.62° in the d2-48h sample (Figure 4.4f).

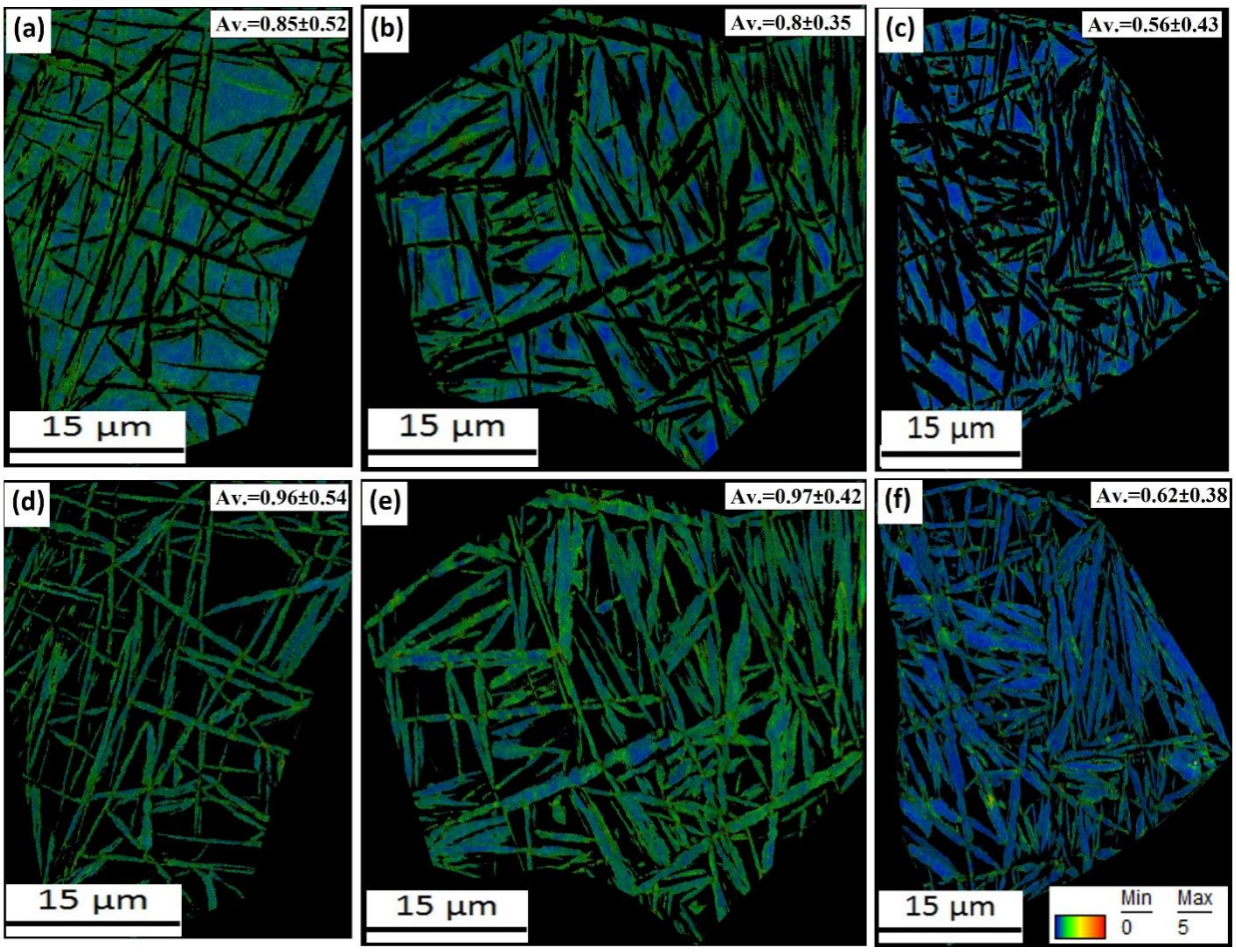

Figure 4.4. *KAM maps of retained austenite phase in (a) D2-25h, (b) D2-33h and (c) D2-48h and of bainite phase in (d) D2-25h, (e) D2-33h and (f) D2-48h samples.*

The TEM BF images of samples D2-25h (Figure 4.5a), D2-33h (Figure 4.5b) and D2-48h (Figure 4.5c) reveal the bainite (αb) and retained austenite phases as marked in the respective figures. In the microstructure of D2-25h (Figure 4.5a), bainitic sheaves are visible, and dark regions inside the sheaves are filmy retained austenite, while the brighter regions represent bainitic subunits. A double arrow line in the figures indicates the width of the bainite sheaf. The size of the sheaf increases with longer austempering time in the D2-33h and D2-48h samples, suggesting that more bainite is formed near previously formed bainite in an autocatalytic manner rather than through grain boundary nucleation. A high-magnification image of the bainite plate in Figure 4.5d shows the precipitation of carbides in the D2-48h sample. The presence of carbide is further confirmed by the selected area diffraction pattern (SADP) shown in Figure 4.5f, corresponding to the bright field image in Figure 4.5e of the D2-48h sample. The d-spacing of the spot circled in the SADP (Figure 4.5f) is 2.5 Å, which could not be identified with any specific carbide as the highest d-spacing of bainite or austenite is less than 2.1 Å.

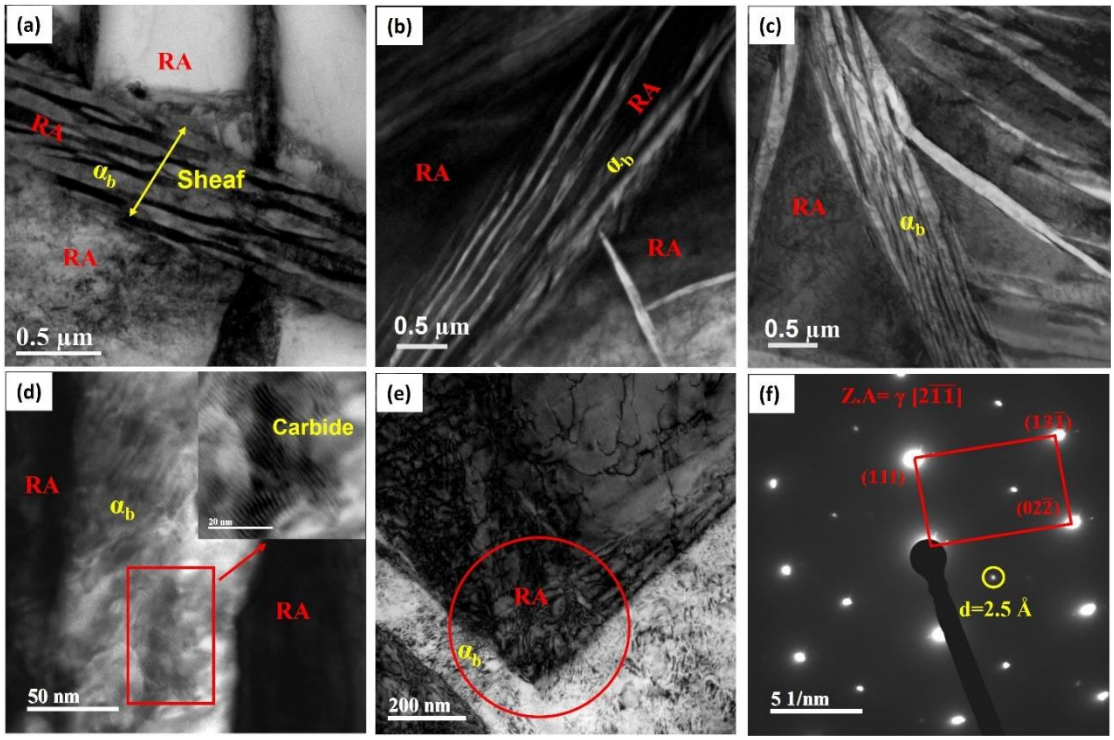

Figure 4.5. *TEM bright-field images of (a) D2-25h, (b) D2-33h, (c, e) D2-48h, (d) magnified view of bainite of D2-48h showing presence of carbides evidenced by the occurrence of Moire fringes and (f) selected area diffraction pattern corresponding to Fig.4.5e (ZA represents zone axis).*

A TEM BF micrograph in Figure 4.6a shows bainite plates of different sizes within a sheaf. The average thickness of plates in the middle of the sheaf is less than 100 nm, but the plates at both edges of the sheaf are abnormally thickened to a size of 229 nm and 456 nm. The abnormal thickening is not observed in the D2-25h and D2-33h samples, as shown in Figures 4.5a and b, respectively. The corresponding diffraction pattern (Figure 4.6c) confirms that austenite (γ) and bainite phases are in the NW orientation relationship, which is also confirmed in the simulated diffraction pattern in Figure. 4.6d. A dark field image (Figure 4.6b) is captured from the marked region on the diffraction pattern, revealing the presence of fine carbides inside the bainite plates. The contrast present inside bainite plates cannot be associated with any dislocations and therefore is assumed to be from the presence of fine carbide particles.

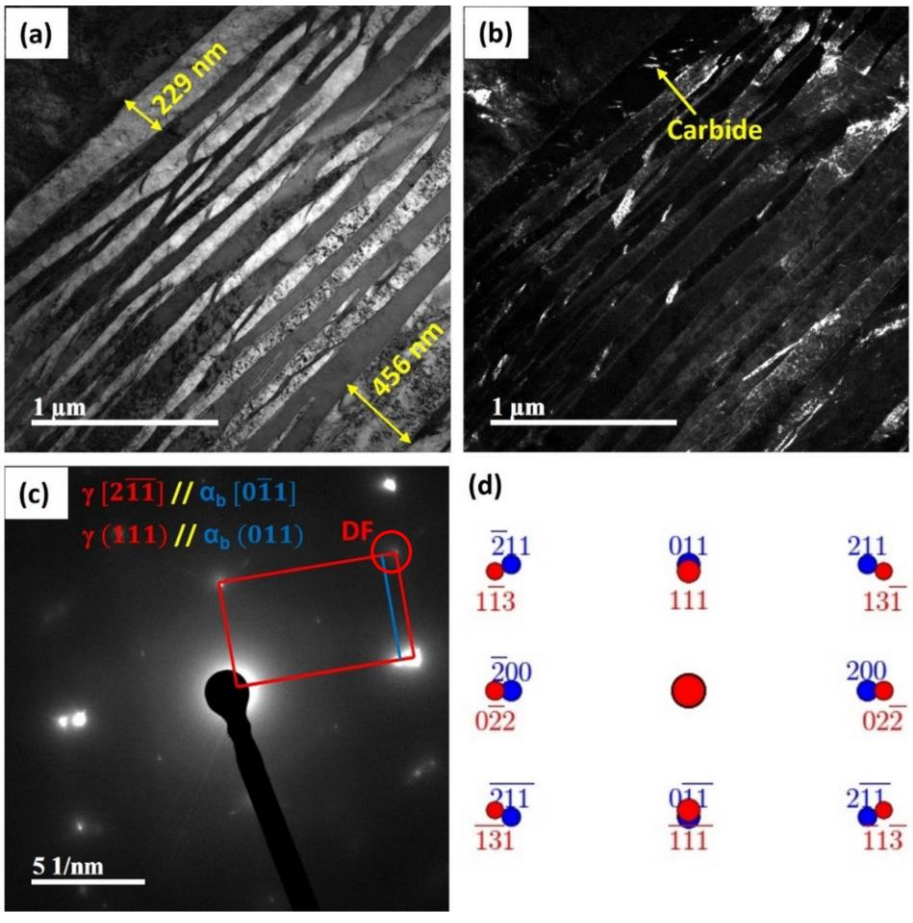

Figure 4.6. *TEM micrographs of D2-48h (a) BF image (b) Dark field image, (c) corresponding diffraction pattern and (d) simulated pattern of* γ $[2\bar{1}\bar{1}]$ *and* α_b $[0\bar{1}1]$ *zone axis.*

Additional TEM analysis is conducted on the D2-48h sample, which reveals the presence of satellite spots around the fundamental reflection in the DP shown in Figure 4.7b, corresponding to the BF image in Figure 4.7a. The zone axis of DP is the same as γ $[2\bar{1}\bar{1}]$ and α_b $[0\bar{1}1]$ as in Figure 4.6. DF images corresponding to positions 1,2 and 3 marked in DP (Figure 4.7b) are shown in Figure 4.7c, d and e, respectively. DF1 and DF2 correspond to RA and bainite, respectively, while DF3 shows the presence of both phases in lower quantities. The satellite spots are observed mainly due to the modulated structure, which has long-range periodicity compared to the original spot.

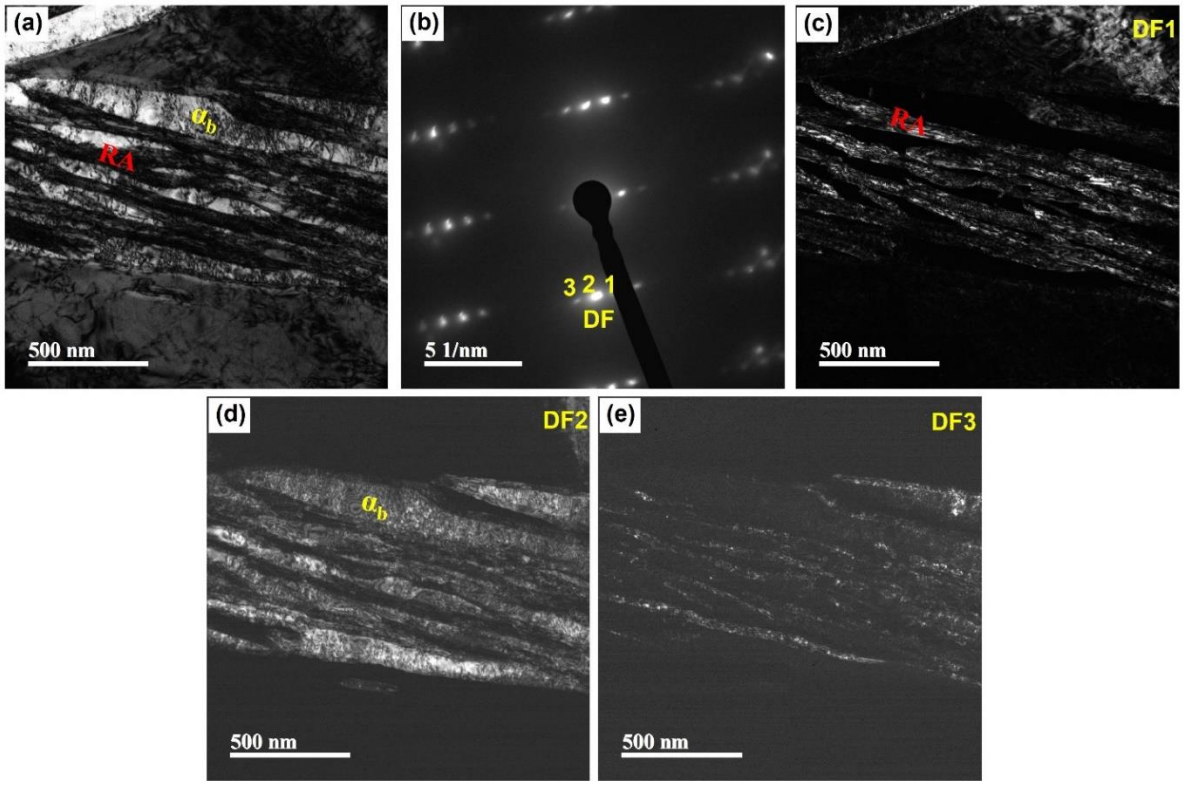

Figure 4.7. *TEM micrographs of D2-48h (a) BF image (b) corresponding diffraction pattern, (c), (d) and (e) are respective dark field images from spots 1, 2 and 3 of DP shown in Figure b.*

The misorientation angle (MA) distribution chart between bainite and austenite is shown in Figures 4.8a, b and c for D2-25h, D2-33h and D2-48h, respectively. The majority of MA fraction is in the range of 42°- 47°, which is the ideal case for K-S (42.85°) and N-W (45.99°) orientation relationships. The samples exhibit both K-S and N-W orientation relationships in almost equal proportions. The MA maps in Figures 4.8d, e and f show a single austenite grain in the magnified form corresponding to the K-S and N-W orientation relationships for D2-25h, D2-33h, and D2-48h, respectively, represented by blue and red lines superimposed on the phase map. These maps confirm the presence of K-S and N-W orientation relationships rather than a specific type of orientation relationship.

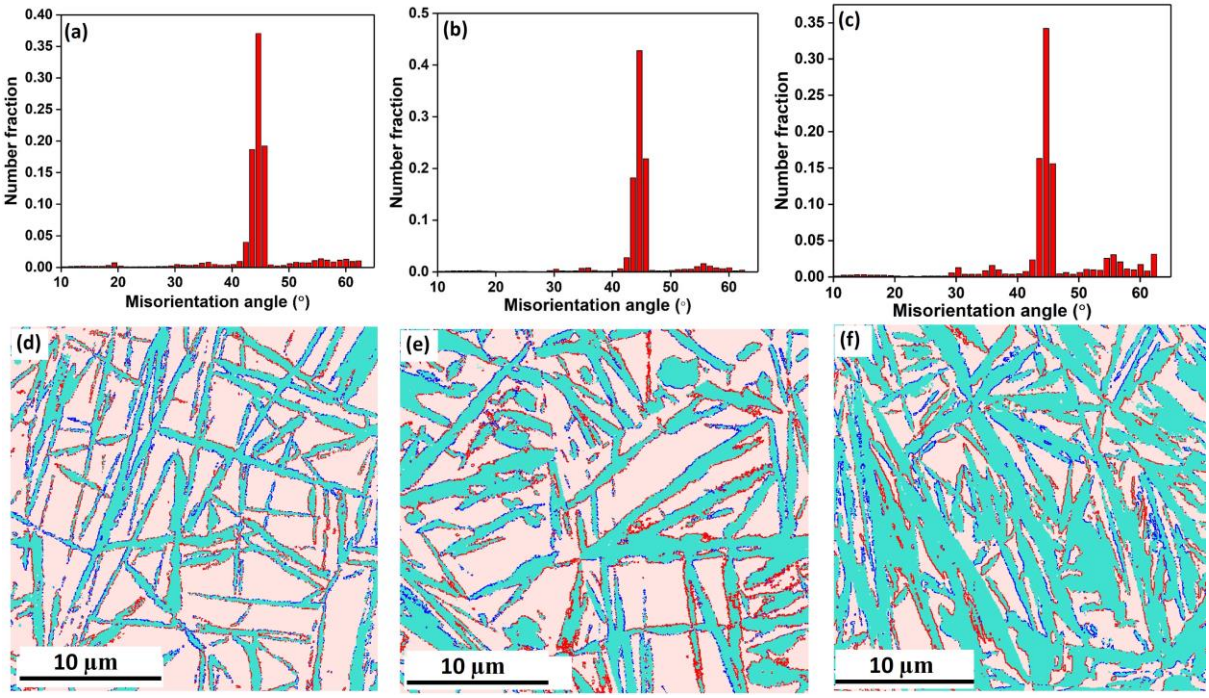

Figure 4.8. *Misorientation angle (MA) chart of (a) D2-25h, (b) D2-33h and (c) D2-48h, misorientation angles corresponding to K-S (blue lines) and N-W (red lines) OR are superimposed on phase map (the pink color is austenite and aqua color is bainite) of (d) D2-25h (e) D2-33h and (f) D2-48h.*

The crystallographic orientation relationship between austenite and bainite is plotted using a quick pole figure map from EBSD scanned data. A single austenite grain is cropped from the original scanned data and the IPF maps of bainite are shown in Figures 4.9a, b and c

for D2-25h, D2-33h and D2-48h, respectively. It should be noted that EBSD cannot detect bainite plates and filmy austenite between them. The observed plate-like features are blocks of bainite, and the black regions in between them are retained austenite. As mentioned, plates inside block have the same orientation, so each color represents a specific variant. The austenite (red-filled circles) and bainite (open black circles) orientations are shown in the pole figure maps (4.9d, e and f) for D2-25h, D2-33h and D2-48h, respectively. The Euler angles of austenite are used to plot variants corresponding to the K-S orientation relationship, and corresponding variant numbers are marked in the figure. It has been confirmed that the initial thickness of the bainite plates is fine in D2-25h, and that on increasing the austempering time, the plates become coarser. The D2-48h sample (Figure 4.9c) demonstrates the thickest blocks due to the sidewise formation of plates. Another notable feature in the D2-48h sample is the formation of blocks with the same crystallographic variant perpendicular to the existing blocks, as shown by the arrow mark in Figure 4.9c. The blocks are from the same packet and variant but differ in their habit planes. As the transformation time increases, variant selection becomes stronger, forming the same orientation plates that are either parallel or making some angle to the existing plates Among the variants formed after 48 hours of transformation, V19 (γ (11$\bar{1}$) || α_b (011), γ [$\bar{1}$10] || α_b ($\bar{1}\bar{1}$1]) is the strongest variant followed by V13 (γ ($\bar{1}$11) || α_b (011), γ [0$\bar{1}$1]) || α_b [$\bar{1}\bar{1}$1]) and V6 (γ (111) || α_b (011), γ [1$\bar{1}$0] || α_b [$\bar{1}$1$\bar{1}$]. The variants V19 and V13 are similar to V1 from a different CP group, and they are present in higher amounts along with V6. In addition to V1 and V6, some amount of twin-related variant, V2, also forms in high carbon nanostructured bainitic steel.

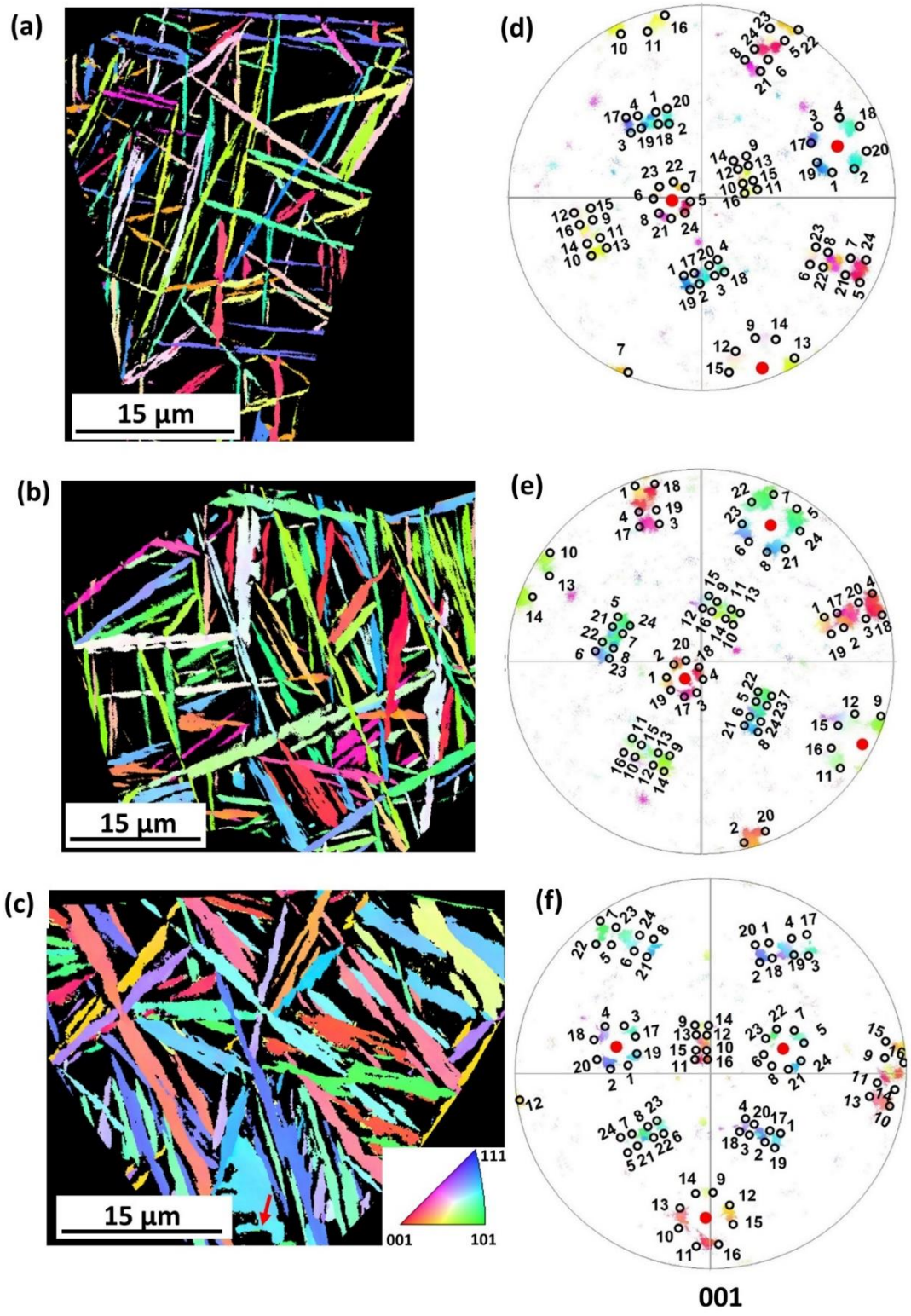

Figure 4.9. *EBSD IPF maps of normal direction of austempered samples of bainite phase (a) D2-25h, (b) D2-33h and (c) D2-48h, {001} pole figure maps showing orientation of austenite (filled red circles) and bainite (open black circles) of (d) D2-25h (e) D2-33h and (f) D2-48h. (Corresponding K-S variant numbers are shown in respective positions).*

4.3 Discussion

In-depth characterization at different austempering times reveals changes in dislocation density and other microstructural features. The effect of time on bainitic transformation is analysed in the present study and are discussed below.

4.3.1 Effect of alloy content and austempering time on the volume fraction of bainite

The results obtained from the experiment show that 35% of bainite is formed after 25 hours of transformation, whereas the TTT diagram calculation based on JMatPro predicts only 10% bainite formation after 27 hours of austempering. It is important to note that the TTT diagram calculation is based on thermodynamic as well as empirical kinetic models, but nucleation of bainite is dependent on additional kinetic factors. The initial stage of transformation is accelerated by the presence of defects in the form of dislocations and grain boundaries. It is sensitive to austenite grain size as these are the preferential nucleation sites for bainite nucleation, and a minor error in grain size measurement may cause discrepancies in final volume fraction calculation using JMatPro. It is also known that pre-deformation (about 10% strain) can accelerate bainite transformation kinetics [185–187] . There is a possibility of inheritance of minor strain from the hot rolling stage, which can accelerate the initial stage of bainitic transformation.

The fraction of bainite formed mainly depends on the alloy composition, austempering temperature, and time. Among different alloying elements, Al and Co accelerate the transformation by increasing the driving force of transformation [131,132], while other elements retard the kinetics. Carbon is the most effective element in retarding the bainite transformation and stabilizing austenite [188]. At a constant temperature, an alloy with a higher mass% of carbon will form a lower volume fraction of bainite, while an alloy with a lower mass% of carbon will form a higher volume fraction of bainite [126]. Mn, Cr and Si also reduce

the driving force for bainitic transformation and retards transformation kinetics [188]. Cementite precipitation is diminished due to a reduction in the driving force by the presence of about 1.5 mass% silicon [72]. But it is not sufficient to stop cementite precipitation in the supersaturated bainite phase of high-carbon steel [66].

Like composition, the thermodynamic effect of temperature on the volume fraction of bainite, is explained earlier by Bhadeshia [126]. Bainitic transformation at a lower temperature will result in the formation of more bainite, while transformation at a higher temperature will reach the T_0 curve earlier, resulting in a lower quantity of bainite formation. Several experiments have been conducted to see the variation in bainite volume fraction with varying temperatures in high-carbon steels [69,131,189]. The amount of bainite formed in high carbon and high silicon steel at 200 °C and 300 °C is studied by Caballero et al. [69]. At 200 °C, no bainite is formed after 24 hours of austempering, and the alloy contains martensite and austenite phases. After 48 hours of transformation, about 35 % of bainite is formed, and the rest are martensite and austenite. On subsequent increasing time, the bainite volume fraction is increased, and no martensite is formed due to suppression of Ms temperature by more carbon enrichment. Austempering at 300 °C for 12 hours forms about 50% volume percent of bainite and no martensite. But interestingly, after 19 hours of transformation, no additional bainite is formed, and the same behavior is observed in 200 °C austempered sample for 144 hours and 240 hours. The same is also observed in the current investigation and is explained based on T_0 and T_0' curves in the subsequent paragraphs.

The current alloy contains 1.06 mass% of carbon, which significantly slows down kinetics, resulting in only 35 volume percent of bainite after 25 hours of transformation. Although it increases to 50% after 33 hours of transformation, interestingly, the percent of bainite transformed reaches only 54% when the time is further increased to 48 hours. The saturation of bainitic transformation is explained on the basis of T_0 and T_0' plots as given in Fig.4.10. It

is expected that the bainitic transformation ceases when the composition of austenite reaches T_0' [75] during transformation.

The T_0 and T_0' temperatures are important parameters for understanding the bainitic transformation process in a given alloy. For a given composition, T_0 is the temperature at which free energy of austenite and bainite phases are equal, while T_0' considers the additional 400 J/mol energy stored in bainite due to diffusionless growth [75]. The carbon concentration corresponding to these temperatures is calculated using MUCG83 software developed by Bhadeshia [190]. The carbon concentrations corresponding to T_0 and T_0' temperatures are found to be 1.43 mass % and 1.09 mass % respectively. The measured carbon concentrations in the retained austenite of the samples (Table 4.1) are lower than the calculated T_0 curve, but slightly higher than the T_0' curve for longer austempered samples (D2-33h and D2-48h) (Fig. 4.10). This suggests that the transformation reached saturation after 33 hours, and further transformation up to 48 hours resulted in some modifications in the microstructure. It is worth noting that there may be some minor errors in the determination of carbon content in the retained austenite, which can slightly affect the accuracy of these calculations.

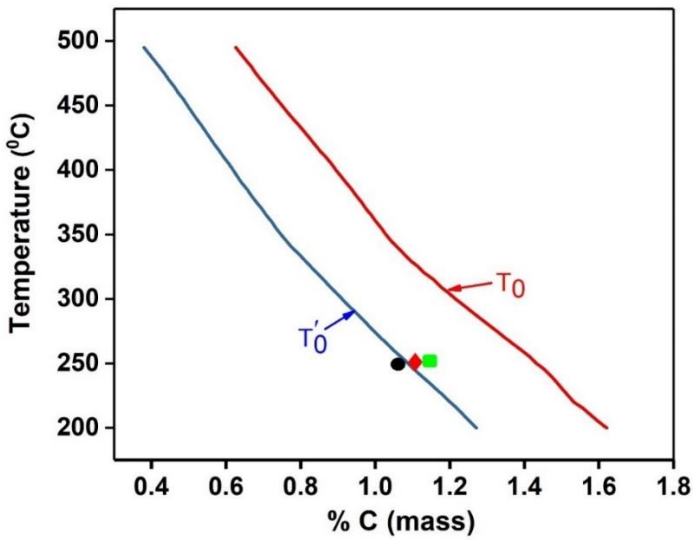

Figure 4.10. *T_0 and T_0' plots using MUCG 83 software. Black circle, red diamond and green square show carbon concentration at 250 °C in RA for D2-25h, D2-33h and D2-48h samples respectively.*

4.3.2 Effect of austempering time on microstructure

Bainite nucleation is believed to follow the displacive theory of transformation, in which the movement of interstitial carbon is a thermally activated process. Dislocations present in the austenite phase dissociate to create a fault, and in the subsequent step, carbon partitions to the surrounding matrix, creating a sufficient driving force for nucleation [191,192]. During the early stage of transformation, there is an adequate driving force for grain boundary nucleation, while in the later stage, the driving force is reduced due to carbon supersaturation [75,193].

In the current study, wider bainitic sheaves are observed after 33 and 48 hours of austempering, compared to 25 hours. Bainitic transformation initially starts with grain boundary nucleation at the required driving force. Grain boundary nucleation leads to autocatalytic nucleation because of stress or strain-induced transformation. Subsequent to bainitic transformation, carbon enrichment in austenite reduces driving force for further grain boundary nucleation, resulting in a decreased nucleation rate due to increased activation energy [194–196]. However, autocatalytic nucleation continues as it requires a lesser driving force. Therefore, although the initial stage of austempering is dominated by grain boundary nucleation, autocatalytic nucleation contributes to the thickening of the bainite sheaves (D2-33h and D2-48h samples) in later stages. Consequently, the width of bainitic sheaves increases due to adding more subunits, mainly by autocatalytic nucleation.

In the D2-25h sample, there is a difference in carbon content between the blocky and filmy retained austenite, which is evident from the asymmetric peak in the XRD pattern of the austenite phase (as shown in Figure 4.3d). However, as the austempering time increases (D2-33h and D2-48h), the XRD peaks become relatively symmetric, indicating a more homogeneous distribution of carbon. There is a discrepancy between the carbon content of the

initial base material and the calculated carbon mass% using XRD in the bainite and austenite phases. The carbon quantity imbalance between the bainite and austenite phases is due to the presence of carbon clusters in these phases. Furthermore, longer austempering times lead to auto-tempering of bainite, resulting in the precipitation of fine carbides and carbon clusters, as shown in Figure 4.5d. The size of the clusters and precipitates is so tiny that it could not be quantified by the characterization technique (TEM) used in the present study. The amount of carbon in the carbide and clusters accounts for the missing mass balance of carbon. Quantifying the amount of carbon from TEM micrographs can be challenging due to their fine size, low volume fraction, and localized information. Additionally, the carbide peak position in XRD patterns can interfere with the (110) peak of bainite and the (111) austenite peak, making it difficult to estimate the amount of carbides, especially when their fraction is low.

The satellite spots observed in Fig. 4.7b are due to carbon clusters. These were previously observed in martensitic steel when aged below 100 °C [197]. This phenomenon is attributed to periodically spaced clusters of carbon atoms smaller than 10 Å. The carbon atoms sit in the c-site of the octahedral void and fluctuate sinusoidally in the (102) planes of martensite. This causes a displacement of iron atoms from their average positions, increasing the intensity of satellite spots [197–199]. Bainitic steel, with a carbon content greater than 0.8 mass%, shows tetragonality due to excess carbon in regular octahedral sites of the bainite phase [200,201]. Analysis of clusters using atom probe tomography in high-carbon bainitic steel reveals the presence of $Fe_{16}C_2$-type clusters in the bainite phase [202]. The presence of clusters in ordered octahedral positions gives rise to a modulated structure. The driving force for clustering is attributed to a reduction in the lattice-distortion strain energy caused by interstitial atoms [203].

4.3.3 Effect of dislocation density on plate and sheaf thickness of bainite

A high amount of dislocations in bainite is inherited from shape deformation during phase change and in RA due to the plastic accommodation of bainitic plates [82]. The calculated dislocation density by the MWH method and qualitative interpretation from EBSD KAM map demonstrate a lower value in austenite and bainite of the D2-48h sample than that of D2-25h and D2-33h samples. If austempering is continued after the transformation reaches the T_0' line, it can result in the rearrangement of dislocations rather than the generation of additional dislocations. A low transformation rate and longer transformation time result in less dislocation density due to the annihilation of some dislocations, as also observed by Lin et al. [204].

As mentioned earlier, the thickness of bainitic plates plays a significant role in the yield strength of the alloy. The average thickness of the plates is measured from SEM secondary electron micrographs for the D2-25h and D2-48h samples, and reported in Table 4.3 after correcting for stereological effects. The thickness of plates is also measured from the bright-field images taken in TEM, with a resolution of 0.2 nm. A total of 10 images, comprising 100 plates of reduced length, are analyzed, and the results are very similar.

In addition to the measurement, the bainite plate thickness is also calculated by a model developed by Yang et al. [79] as given in Equation 4.1.

$$t_b = 222 + 0.01242 \times T_{iso} + 0.01785 \times \Delta G^{\gamma \to \alpha} - 0.5323 \times \sigma_{IT}^{\gamma} \qquad (4.1)$$

In the equation, t_b represents the thickness of the bainite plate (nm), T_{iso} is the isothermal transformation temperature (°C), $\Delta G^{\gamma \to \alpha}$ is the chemical driving force (J/mol) for austenite to bainite transformation and σ_{IT}^{γ} is the yield strength (MPa) of the austenite at the transformation temperature. The chemical driving force for the austenite to bainite transformation is calculated using MUCG83 software. The yield strength of the austenite at room temperature,

σ_{RT}^{γ} , is calculated using Equation 4.2 as given by Bohemen [80]. The yield strength of the austenite at the isothermal temperature, σ_{IT}^{γ}, is also estimated using the calculated value of σ_{RT}^{γ} and Equation 4.3.

$$\sigma_{RT}^{\gamma} = 87.8 + 254w_c + 15.1w_{Si} + 2.5\, w_{Cr} + 14.5w_{Mo} + 5.4w_{Al} + 10.5/\sqrt{d^{\gamma}} \qquad (4.2)$$

$$\sigma_{IT}^{\gamma} = \sigma_{RT}^{\gamma}\left(1 - \frac{2.2(T-25)}{10^3} + \frac{4.2(T-25)^2}{10^6} - \frac{3(T-25)^3}{10^9}\right) \qquad (4.3)$$

(The italics font could not be converted to roman font using Equation editor of MS office)

In the equation, w_{Si}, w_{Cr}, w_{Al}, w_{Mo} are mass percentages of Si, Cr, Al, and Mo respectively. The carbon content (w_c) in the austenite is taken as calculated from XRD and d^{γ} represents the average austenite grain size. From the austenite YS (Equations 4.2, 4.3), and the driving force (MUCG 83), bainite plate thicknesses are calculated (using Equation 4.1) to be 102.2 nm and 93.7 nm for D2-25h and D2-48h samples, respectively (Table 4.3). However, the calculated thickness data significantly deviates from the respective measured values for both samples. The estimated average plate thickness value is more than the measured value. The mismatch between calculated and experimental values is mainly due to two reasons. Firstly, the bainitic transformation is a dynamic process, and parameters such as austenite YS and its grain size continuously change with the progress of transformation. Most of the earlier equations assume it to be a static process [77,80]. Secondly, plate thickness mainly depends on the YS of austenite, which is calculated by neglecting the contribution of dislocation density [79]. But in reality, at the early stage of transformation, the formation of bainite plates leads to the generation of dislocations in the austenite phase. The contribution of dislocation density (σ_{dis}^{γ}) towards austenite YS is given by Equation 4.4 [205].

$$\sigma_{dis}^{\gamma} = M_t \alpha \mu b \sqrt{\rho^{\gamma}} \qquad (4.4)$$

where M_t is the Taylor factor, α is a constant and μ is the shear modulus. Before the start of bainitic transformation, dislocation density in austenite is of the order of $10^{11}/m^2$ [206] but as the transformation proceeds, more dislocations are generated in the austenite phase. Apart from dislocation density, austenite available for the formation of bainite plates decreases dynamically with transformation. These two factors mainly contribute towards the deviation of the calculated bainite plate thickness from the measured value.

Table 4.3. Calculated and measured bainite plate thickness data.

Sample	Driving force (J/mol)	yield strength of austenite (MPa)	Plate thickness calculated (nm) (t_b)	Plate thickness measured (nm) (t_m)
D2-25h	2242	306	102.2	51±18
D2-48h	2216	321	93.7	65±34

The above section describes factors like yield strength, driving force and austenite grain size that affect the thickness of a plate. As the transformation progresses, dislocation accumulation in retained austenite increases, it should reduce the rate of bainite plate thickening. The plate thickness can continue to increase even after length is halted till the chemical driving force is balanced by opposing strain energy in austenite [207]. But unlike the above theory, as the transformation progresses, abnormal thickening is observed at both edges of the sheaves (D2-48h) as shown in Fig.4.6a. The rate of thickening of plates at the edges is due to the absence of parallel plates in other words hard impingement [207,208]. The probability of hard impingement is higher at the initial transformation stage, which reduces in the later stage.

Apart from this factor, two more observations are made in the current study. First one is the reduction in dislocation density in austenite, as observed in the KAM map and from a quantitative XRD analysis calculation. Second is the increase in driving force due to the depletion of carbon by carbide precipitation in bainite. The plates in the middle portion are already in thermoelastic equilibrium, so they cannot grow further, but the plates at the edges

grow freely due to the reduction in resistance by obstacles from dislocations and increased chemical driving force.

Based on the discussion, it can be inferred that it is necessary to incorporate an additional parameter related to the dislocation density to improve the accuracy of empirical equations in predicting bainite plate thickness.

4.3.4 Effect of austempering time on crystallographic variant selection

The phenomenon of crystallographic variant selection has been extensively studied for martensitic steel and has also been applied to bainitic steel due to their similar transformation behavior [209–211]. In low-carbon steel, martensite blocks consist of a few variants (V1-V4) with low misorientation angles, while in high-carbon steel, all six variants are observed rather than a specific variant [90]. There is less tendency for subunit formation in high-carbon martensite, whereas the opposite occurs in low-carbon martensite [88]. It has been observed that the V1-V16 type variant dominates in high-carbon steel.

Most of the variant selection in bainitic steel is studied at higher temperatures (upper bainite). It is observed that the variant pairing occurs within the same CP group (V1–V6). Bainite transformed at 500 °C inside a packet consists of only two variants (V1 and V4) with a small misorientation between them, while a packet formed at 400 °C consists of all six variants in the same CP group [97]. Another significant observation related to OR and variant selection at different temperatures is made by Takayama et al. [89]. It is concluded in their work that exact K-S OR is not observed in bainite or martensitic steel. The angular deviation of the close-packed planes between bainite and austenite increases with temperature, whereas it decreases for the close packed direction. Three variant pairs are observed in medium carbon steel at different austempering temperatures [212]. The variants V1-V6 are formed at low temperatures, V1-V2 at intermediate temperatures, and V1-V4 at high temperatures. Variant

selection in nanostructured bainite at various temperatures [95] reveals that decreasing austempering temperature weakens variant selection, and the reverse is observed at higher temperatures. The effect of carbon concentration on variant selection for martensite and bainite is observed to be opposite in nature [97]. Lower carbon concentration at low temperatures results in weak variant selection in bainite, whereas it is the reverse in the case of martensite. Lower carbon concentration (0.2 mass%) at 400 °C results in a single variant, whereas high carbon concentration (more than 0.2 mass%) results in multiple variants [213]. The observed multivariant formation at the grain boundaries at 400 °C is believed to be due to higher austenite yield strength arising from high carbon content.

A fast multiscale clustering method in MTEX, developed by Nyyssonen et al. [214], determines the variant pairing in the current studied austempered samples. The fraction of variant pairing (V1-V24) relative to V1 is demonstrated in Figure 4.11a, b and c for D2-25h, D2-33h and D2-48h, respectively. The variant pair, V1-V6 is the dominant pair over others in all the samples, and the fraction also increases from D2-25h to D2-48h.

Grain boundaries play a crucial role in the initial stage of transformation, particularly in the formation of a specific variant of bainite [213]. However, as the transformation advances, the importance of grain boundaries diminishes, and autocatalytic nucleation becomes more significant. The selection of variants is influenced by the driving force and the austenite yield strength. High yield strength of austenite and driving force for bainite transformation aid in the formation of multivariant bainite [95,97]. Furthermore, plastic accommodation during the later stages of transformation favors the formation of identically oriented plates [94,97]. During the initial stage of transformation (D2-25h), a higher driving force helps in grain boundary nucleation, forming fine blocks of different variants. As transformation progresses (D2-48h), the driving force decreases due to carbon partition into austenite, and yield strength reduces due to dislocation annihilation, facilitating the unobstructed growth of V1-V6 variant pair.

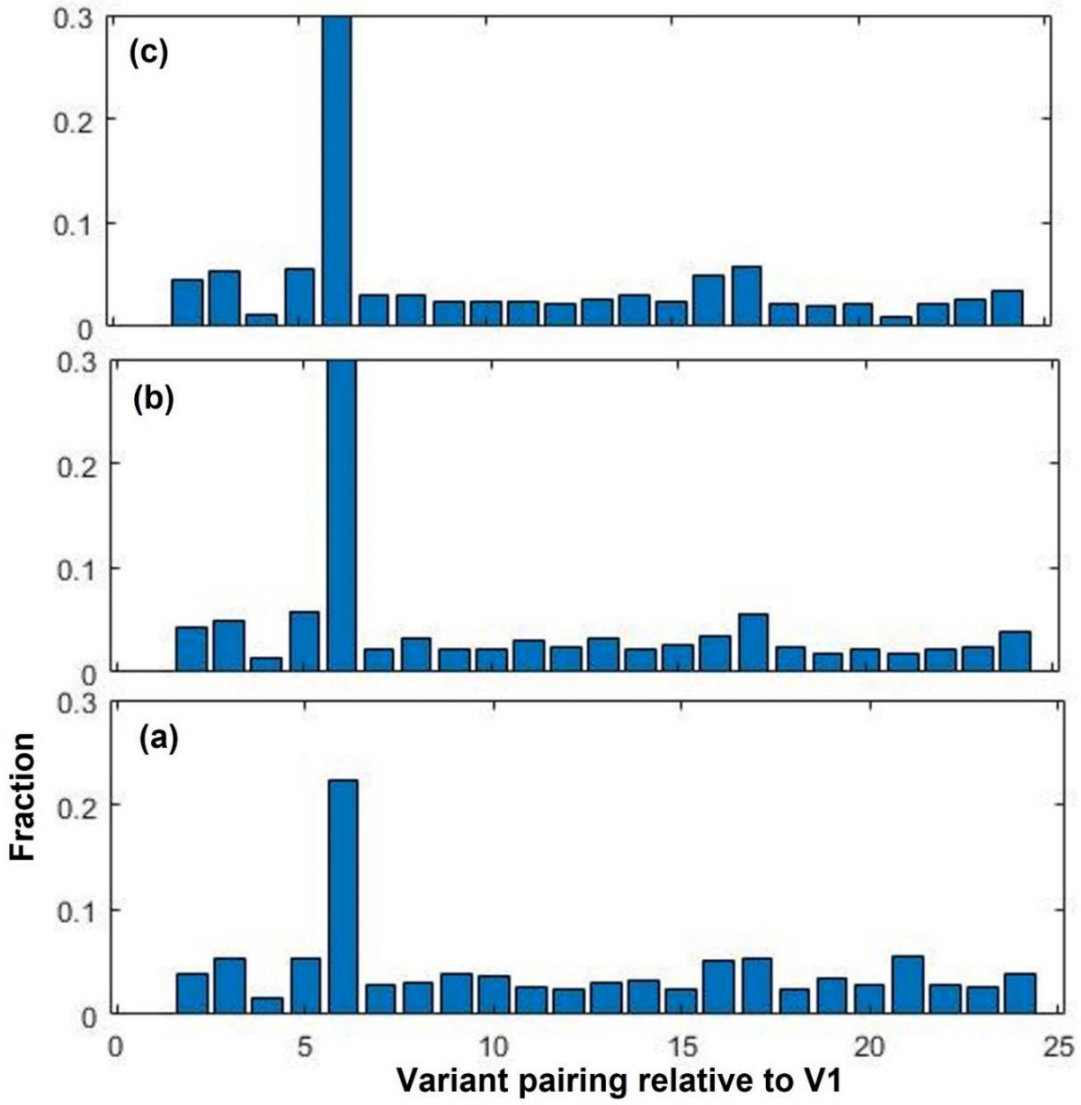

Figure 4.11. *Variant pairing with respect to V1 for (a) D2-25h (b) D2-33h and (c) D2-48h.*

4.4 Conclusions

Austempering of the designed Fe-1.06%C-2.1%Si-2.08%Mn-1.3%Cr-0.28%Mo-1.2%Al-1.5%Co-0.44%Ni alloy produces nano bainite with a high amount of retained austenite. Microstructural analysis using different techniques leads to the following conclusions:

- Austempering of metastable austenite for a longer period leads to saturation of bainite transformation and partial annihilation of dislocations.
- At an early stage of bainitic transformation, there is a continuous decrease in austenite grain size and an increase in dislocation density, which enhances the yield strength. However,

this adversely affects the growth of bainite plates, resulting in a decrease in the rate of bainite plate thickening. The overestimation in calculated plate thickness is likely due to the omission of dynamic data on austenite grain size and dislocation density.

- At a later stage, as the transformation progress, dislocations in the austenite phase are partially annihilated due to slower kinetics. The reduction in dislocation density in austenite and lowering of hard impingement, increases the thickness of bainite plates at the edge of a sheaf.
- Instead of forming a single orientation relationship, the bainite formed at 250 °C consists of both Kurdjumov–Sachs and Nishiyama–Wasserman types.
- The crystallographic variant pairs V1-V6, related to Kurdjumov–Sachs orientation relationship dominate over others as the transformation progresses.